

## POLARIZED FOREGROUND POWER SPECTRA FROM THE HERA-19 COMMISSIONING ARRAY

SAUL A. KOHN,<sup>1</sup> JAMES E. AGUIRRE,<sup>1</sup> PAUL M. CHICHURA,<sup>1</sup> AUSTIN F. FORTINO,<sup>1</sup> AMY S. IGARASHI,<sup>1,2</sup> ROSHAN K. BENEFO,<sup>1</sup> TASHALEE S. BILLINGS,<sup>1</sup> SAMAVARTI GALLARDO,<sup>1,3</sup> PAUL LA PLANTE,<sup>1</sup> ZACHARY E. MARTINOT,<sup>1</sup> CHUNEETA D. NUNHOKEE,<sup>4,1</sup> PAUL ALEXANDER,<sup>5</sup> ZAKI S. ALI,<sup>6</sup> ADAM P. BEARDSLEY,<sup>7,8</sup> GIANNI BERNARDI,<sup>9,4,10</sup> JUDD D. BOWMAN,<sup>7</sup> RICHARD F. BRADLEY,<sup>11</sup> CHRIS L. CARILLI,<sup>12,5</sup> CARINA CHENG,<sup>6</sup> DAVID R. DEBOER,<sup>6</sup> ELOY DE LERA ACEDO,<sup>5</sup> JOSHUA S. DILLON,<sup>6,8</sup> AARON EWALL-WICE,<sup>13,14</sup> GCOBISA FADANA,<sup>15</sup> NICOLAS FAGNONI,<sup>5</sup> RANDALL FRITZ,<sup>15</sup> STEVE R. FURLANETTO,<sup>16</sup> BRIAN GLENDENNING,<sup>12</sup> BRADLEY GREIG,<sup>17</sup> JASPER GROBBELAAR,<sup>10</sup> BRYNA J. HAZELTON,<sup>18,19</sup> JACQUELINE N. HEWITT,<sup>20</sup> JACK HICKISH,<sup>6</sup> DANIEL C. JACOBS,<sup>7</sup> AUSTIN JULIUS,<sup>10</sup> MACCALVIN KARISEB,<sup>10</sup> NICHOLAS S. KERN,<sup>6</sup> MATTHEW KOLOPANIS,<sup>21,7</sup> TELALO LEKALAKE,<sup>10</sup> ADRIAN LIU,<sup>6,22</sup> ANITA LOOTS,<sup>10</sup> DAVID MACMAHON,<sup>6</sup> LOURENCE MALAN,<sup>10</sup> CRESSHIM MALGAS,<sup>10</sup> MATTHYS MAREE,<sup>10</sup> NATHAN MATHISON,<sup>10</sup> EUNICE MATSETELA,<sup>10</sup> ANDREI MESINGER,<sup>17</sup> MIGUEL F. MORALES,<sup>18</sup> ABRAHAM R. NEBEN,<sup>20</sup> BOJAN NIKOLIC,<sup>5</sup> AARON R. PARSONS,<sup>6</sup> NIPANJANA PATRA,<sup>6</sup> SAMANTHA PIETERSE,<sup>10</sup> JONATHAN C. POBER,<sup>23</sup> NIMA RAZAVI-GHODS,<sup>5</sup> JON RINGUETTE,<sup>18</sup> JAMES ROBNETT,<sup>12</sup> KATHRYN ROSIE,<sup>10</sup> RADDWINE SELL,<sup>10</sup> CRAIG SMITH,<sup>10</sup> ANGELO SYCE,<sup>10</sup> MAX TEGMARK,<sup>20</sup> NITHYANANDAN THYAGARAJAN,<sup>12,7,24</sup> PETER K. G. WILLIAMS,<sup>25</sup> AND HAOXUAN ZHENG<sup>20</sup>

<sup>1</sup>Center for Particle Cosmology, Department of Physics and Astronomy, University of Pennsylvania, Philadelphia, PA 19104 USA

<sup>2</sup>Department of Astronomy, San Diego State University, San Diego, CA 92182 USA

<sup>3</sup>California State University of Los Angeles, 5151 State University Dr, Los Angeles, CA 90032 USA

<sup>4</sup>Department of Physics and Electronics, Rhodes University, PO Box 94, Grahamstown, 6140, South Africa

<sup>5</sup>Cavendish Astrophysics, University of Cambridge, Cambridge, UK

<sup>6</sup>Department of Astronomy, University of California, Berkeley, CA

<sup>7</sup>School of Earth and Space Exploration, Arizona State University, Tempe, AZ

<sup>8</sup>NSF Astronomy and Astrophysics Postdoctoral Fellow

<sup>9</sup>INAF-Istituto di Radioastronomia, via Gobetti 101, 40129, Bologna, Italy

<sup>10</sup>SKA SA, 3rd Floor, The Park, Park Road, Pinelands, 7405, South Africa

<sup>11</sup>National Radio Astronomy Observatory, Charlottesville, VA

<sup>12</sup>National Radio Astronomy Observatory, Socorro, NM

<sup>13</sup>Jet Propulsion Laboratory, 4800 Oak Grove Dr, Pasadena, CA

<sup>14</sup>Dunlap Institute for Astronomy and Astrophysics, Toronto, Ontario, Canada

<sup>15</sup>SKA-SA, Cape Town, South Africa

<sup>16</sup>Department of Physics and Astronomy, University of California, Los Angeles, CA

<sup>17</sup>Scuola Normale Superiore, Pisa, Italy

<sup>18</sup>Department of Physics, University of Washington, Seattle, WA

<sup>19</sup>eScience Institute, University of Washington, Seattle, WA

<sup>20</sup>Department of Physics, Massachusetts Institute of Technology, Cambridge, MA

<sup>21</sup>Department of Physics, Arizona State University, Tempe, AZ

<sup>22</sup>Hubble Fellow

<sup>23</sup>Department of Physics, Brown University, Providence, RI

<sup>24</sup>Jansky Fellow

<sup>25</sup>Harvard-Smithsonian Center for Astrophysics, Cambridge, MA

## ABSTRACT

Foreground power dominates the measurements of interferometers that seek a statistical detection of highly-redshifted HI emission from the Epoch of Reionization (EoR). The inherent spectral smoothness of synchrotron radiation, the

Corresponding author: James E. Aguirre

jaguirre@sas.upenn.edu

dominant foreground emission mechanism, and the chromaticity of the instrument allows these experiments to delineate a boundary between spectrally smooth and structured emission in Fourier space (the “wedge” or “pitchfork”, and the “EoR Window”, respectively). Faraday rotation can inject spectral structure into otherwise smooth polarized foreground emission, which through instrument effects or miscalibration could possibly pollute the EoR Window. Using data from the Hydrogen Epoch of Reionization Array (HERA) 19-element commissioning array, we investigate the polarization response of this new instrument in the power spectrum domain. We confirm the expected structure of foreground emission in Fourier space predicted by Thyagarajan et al. (2015a, 2016) for a HERA-type dish, and detect polarized power within the pitchfork. Using simulations of the polarized response of HERA feeds, we find that almost all of the power in Stokes Q, U and V can be attributed to instrumental leakage effects. Power consistent with noise in the EoR window suggests a negligible amount of spectrally-structured polarized power, to the noise-levels attained. This lends confidence to deep integrations with HERA in the future, but with a lower noise floor these future studies will also have to investigate their polarized response.

*Keywords:* cosmology: observations - dark ages, reionization, first stars – instrumentation: interferometers – techniques: interferometric – polarization

## 1. INTRODUCTION

Many low-frequency (50 – 200 MHz) radio interferometers (e.g. LOFAR<sup>1</sup>, MWA<sup>2</sup>, PAPER<sup>3</sup>, HERA<sup>4</sup>) around the world are seeking to detect brightness-temperature fluctuations of neutral hydrogen during the Epoch of Reionization (EoR; for an overview see Furlanetto et al. (2006)). Such a detection is predicted to be rich in information about the astrophysics and cosmology of the high-redshift ( $\sim 7 < z < 14$ ) Universe. The HI brightness-temperature fluctuations are not only intrinsically faint but also hidden by foreground emission. Foreground emission, predominantly in the form of Galactic and extragalactic synchrotron emission, is many orders of magnitude more powerful than the cosmological signal (e.g. Bernardi et al. 2009a; Pober et al. 2013; Dillon et al. 2014).

Most foreground emission is due to synchrotron emission, which is spectrally smooth. The instrumental response of an interferometer is inherently chromatic, and the cosmological signal is spectrally structured. In sum, this leads to the property that Fourier transforming the interferometric measurement along the frequency axis delineates a boundary in the  $\mathbf{k}$ -space between the **spectrally smooth** foregrounds (in the ‘wedge’) **and** the cosmological HI signal (in the ‘EoR window’) (Datta et al. 2010; Morales et al. 2012; Parsons et al. 2012b,a; Trott et al. 2012; Vedantham et al. 2012; Pober et al. 2013; Thyagarajan et al. 2013; Pober et al. 2014; Liu et al. 2014a,b; Dillon et al. 2015b,a; Thyagarajan et al. 2015a,b). Thermal noise is present throughout this space, and dominates the EoR window in any single observation. Detection of the EoR thus requires long observing seasons, precision calibration, and suppression of instrument systematics.

**The cosmological signal is strongly unpolarized** (Mishra & Hirata 2017). However, polarized synchrotron radiation represents a potential foreground contaminant capable of leaking into the EoR window. At low frequencies, Faraday rotation can impart significant spectral structure to polarized emission (e.g. Moore et al. 2013). This polarized signal is able to ‘leak’ into unpolarized measurements due to miscalibration and instrumental effects (Carozzi & Woan 2009; Geil et al. 2011; Moore et al. 2013; Asad et al. 2015, 2016; Kohn et al. 2016; Nunhokee et al.

2017). Its spectrally-structured nature would alias power into the EoR window.

It is important to constrain intrinsic and leaked polarized signal for any HI intensity mapping experiment. The objective of this paper is an exploration of eight nights of data from the Hydrogen Epoch of Reionization Array (HERA) 19-element commissioning array, coupled with simulations of the instrument, in order to **characterize the polarized response of this interferometer**. One of the more difficult features of an interferometer to characterize is the frequency- and direction-dependent polarized antenna response, which is important for characterizing polarized-to-unpolarized leakage in the wedge/window paradigm (Moore et al. 2017; Nunhokee et al. 2017; Martinot et al. 2018). In this work, we were primarily sensitive to leakage in the unpolarized-to-polarized direction. Due to the symmetry of leakage modes (elaborated upon in Section 2), this still represents a useful constraint on polarized instrument response. This work also represents the first power spectra analysis from HERA. While we did not obtain new upper limits on the EoR power spectrum, we integrated deep enough to test models of the instrument’s spectral response against simulations, and found that they agreed well to the noise levels probed.

This work is organized as follows: in Section 2 we review the theory behind polarization leakage into unpolarized signal and simulate the effects **due to the polarized primary beam** for a model of HERA. In Section 3 we describe the HERA data that we used, its calibration and reduction to power spectra. We present our results, and discuss the implications for HERA’s EoR measurements in Section 4, and conclude in Section 10. We assume the cosmological parameters reported by Planck Collaboration et al. (2016) throughout.

## 2. LEAKAGE MODES

A radio interferometer measures correlations of voltages. Viewed in transmission, a dipole arm of antenna  $i$  radiates a far-field electric field pattern

$$\vec{E}_i(\hat{s}, \nu) = E_{i,\theta}(\nu)\hat{\theta} + E_{i,\phi}(\nu)\hat{\phi} \quad (1)$$

where  $(\hat{\theta}, \hat{\phi})$  define an orthogonal coordinate system on the sphere. These far-field beam patterns, by the reciprocity theorem, define the response of the feed to an electric field from infinity in the direction  $(\theta, \phi)$ .

We may choose to express the electric field response in Right Ascension and Declination basis (unit vectors

<sup>1</sup> [www.lofar.org](http://www.lofar.org)

<sup>2</sup> [www.mwatelescope.org](http://www.mwatelescope.org)

<sup>3</sup> [eor.berkeley.edu](http://eor.berkeley.edu)

<sup>4</sup> [www.reionization.org](http://www.reionization.org)

$\hat{e}_\alpha, \hat{e}_\delta$ ), allowing us to express the coherency tensor field

$$\begin{aligned} \mathcal{C} = & \langle E_\delta^* E_\delta \rangle \hat{e}_\delta \otimes \hat{e}_\delta + \langle E_\alpha^* E_\delta \rangle \hat{e}_\alpha \otimes \hat{e}_\delta \\ & + \langle E_\delta^* E_\alpha \rangle \hat{e}_\delta \otimes \hat{e}_\alpha + \langle E_\alpha^* E_\alpha \rangle \hat{e}_\alpha \otimes \hat{e}_\alpha \end{aligned} \quad (2)$$

where we have dropped the explicit  $(\hat{s}, \nu)$  dependence of the fields. By definition, the coherency field is specified by the Stokes parameters

$$\mathcal{C} = \begin{pmatrix} I(\hat{s}, \nu) + Q(\hat{s}, \nu) & U(\hat{s}, \nu) - iV(\hat{s}, \nu) \\ U(\hat{s}, \nu) + iV(\hat{s}, \nu) & I(\hat{s}, \nu) - Q(\hat{s}, \nu) \end{pmatrix}. \quad (3)$$

Each polarized feed  $p$  of antenna  $i$  responds to incident radiation from direction  $(\hat{\theta}, \hat{\phi})$  with a complex vector antenna pattern

$$\vec{A}_i^p(\hat{s}, \nu) = A_{i,\theta}^p(\hat{s}, \nu)\hat{\theta} + A_{i,\phi}^p(\hat{s}, \nu)\hat{\phi}. \quad (4)$$

The antenna patterns can be written as components of a direction-dependent Jones matrix for a dipole feed  $i$  with arms  $p$  and  $q$ :

$$\mathcal{J}_i = \begin{pmatrix} A_{i,\theta}^p(\hat{s}, \nu) & A_{i,\phi}^p(\hat{s}, \nu) \\ A_{i,\theta}^q(\hat{s}, \nu) & A_{i,\phi}^q(\hat{s}, \nu) \end{pmatrix}. \quad (5)$$

We can then express the fully-polarized visibility equation for the correlation of feeds  $i$  and  $j$  as

$$V_{ij} = \int \mathcal{J}_i \mathcal{C} \mathcal{J}_j^\dagger \exp(-2\pi i \nu \vec{b} \cdot \hat{s}/c) d\Omega = \begin{pmatrix} V_{ij}^{nn} & V_{ij}^{ne} \\ V_{ij}^{en} & V_{ij}^{ee} \end{pmatrix} \quad (6)$$

where we have denoted dipole arms  $p$  and  $q$  as  $n$  and  $e$ , representing a configuration where the arms are oriented along the North-South and East-West directions, respectively.

Unless  $\mathcal{J}$  is both diagonal and, at any given point on the sphere, the diagonal elements are equal, there will be mixing or ‘leaking’ different Stokes parameters together into each element of  $\mathcal{V}$  in a direction dependent way (Geil et al. 2011; Smirnov 2011a,b; Nunhokee et al. 2017).

### 2.1. Direction-Dependent Leakage

The cosmological signal of interest for 21cm cosmology studies is effectively unpolarized, and we therefore use the pseudo-Stokes<sup>5</sup>  $I$  visibility to measure it;

<sup>5</sup> We use “pseudo-Stokes” to refer to Stokes parameters formed from visibilities throughout this work, as they are proxies for the real “Stokes parameters” as defined by the IEEE (Ludwig 1973; van Straten et al. 2010).

$V^I = V^{nn} + V^{ee}$ , which is the trace of  $\mathcal{V}$  (e.g. Moore et al. 2013):

$$\begin{aligned} V_{ij}^I(\nu) &= \text{Tr}(\mathcal{V}_{ij}) = \int \text{Tr}(\mathcal{J}_i \mathcal{C} \mathcal{J}_j^\dagger) \exp(-2\pi i \nu \vec{b} \cdot \hat{s}/c) d\Omega \\ &= \int (\mathcal{M}_{00} I + \mathcal{M}_{01} Q + \mathcal{M}_{02} U + \mathcal{M}_{03} V) \exp(-2\pi i \nu \vec{b} \cdot \hat{s}/c) d\Omega \end{aligned} \quad (7)$$

where  $I$ ,  $Q$ ,  $U$  and  $V$  are the true Stokes sky and are functions of direction and frequency, and  $\mathcal{M}_{ab}(\hat{s}, \nu)$  are the instrumental Mueller matrix elements:

$$\mathcal{M}_{ab}(\hat{s}, \nu) = \text{Tr}(\sigma_a \mathcal{J} \sigma_b \mathcal{J}^\dagger) \quad (8)$$

and  $\sigma_i$  are the Pauli matrices (where the indices are reordered from the quantum mechanical convention to an order which gives the ordering of the Stokes vector as  $(I, Q, U, V)$ ). See Shaw et al. 2015).

We simulated the HERA feed, faceted parabolic dish and analog signal chain using CST<sup>6</sup> to generate the complex  $\vec{E}$ -field receptivity patterns, as described in Fagnoni & de Lera Acedo (2016) (also see public [HERA Memo #21](#)), and then formed  $\mathcal{J}$  and  $\mathcal{M}$  as described above. Examples of  $\mathcal{M}_{ij}$  at 120 MHz and 160 MHz (our low and high bands of interest; see Section 3.2) are shown in Figure 1, projected in the RA/Dec basis. Note that this basis has a singularity at the South Pole, leading to wide-field asymmetries in  $Q$  and  $U$ . Due to the large spread in dynamic ranges between  $\mathcal{M}_{00}$ , other diagonal terms and off-diagonal terms, we use separate color maps for each. All of the dynamic ranges are normalized to the peak of  $\mathcal{M}_{00}$ , which is 1 at zenith. The off-diagonal terms are 2- to 8-orders of magnitude less than the diagonal terms.

The key for these matrices are the mappings of Stokes parameters into pseudo-Stokes visibilities, following

$$\mathcal{M}_{ab}(\hat{s}, \nu) = \begin{pmatrix} I \rightarrow V^I & I \rightarrow V^Q & I \rightarrow V^U & I \rightarrow V^V \\ Q \rightarrow V^I & Q \rightarrow V^Q & Q \rightarrow V^U & Q \rightarrow V^V \\ U \rightarrow V^I & U \rightarrow V^Q & U \rightarrow V^U & U \rightarrow V^V \\ V \rightarrow V^I & V \rightarrow V^Q & V \rightarrow V^U & V \rightarrow V^V \end{pmatrix} \quad (9)$$

<sup>6</sup> [www.cst.com](http://www.cst.com)

where pseudo-Stokes visibilities are formed as:

$$\begin{pmatrix} V^I \\ V^Q \\ V^U \\ V^V \end{pmatrix} = \frac{1}{2} \begin{pmatrix} 1 & 0 & 0 & 1 \\ 1 & 0 & 0 & -1 \\ 0 & 1 & 1 & 0 \\ 0 & -i & i & 0 \end{pmatrix} \begin{pmatrix} V^{nn} \\ V^{ne} \\ V^{en} \\ V^{ee} \end{pmatrix}. \quad (10)$$

At low frequencies and the large scales probed by many low frequency interferometers, Stokes I is extremely bright compared to the other Stokes parameters (Bernardi et al. 2009b, 2010; Jelić et al. 2014, 2015; Asad et al. 2015; Kohn et al. 2016; Lenc et al. 2017; Moore et al. 2017). Moreover, only a few polarized point sources have been observed at frequencies below 300 MHz (Bernardi et al. 2013; Asad et al. 2016; Lenc et al. 2017). Farnes et al. (2014) showed evidence for systematic depolarization of steep-spectrum point sources towards low frequencies, causing low polarization fractions ( $\ll 1\%$ ) below 300 MHz.

These factors make the first column of  $\mathcal{M}$ , which represents  $I \rightarrow I, Q, U, V$ , the most interesting for low-frequency polarized power spectra, since with limited calibration we can expect leakage from Stokes I into the other Stokes parameters to dominate over Stokes Q, U and V emission alone. We proceeded to simulate  $\mathcal{V}$  using our fully-polarized formalism for the HERA-19 commissioning array, described below, using an unpolarized model of the low frequency sky from the Global Sky Model (GSM; de Oliveira-Costa et al. 2008; Price 2016; Zheng et al. 2017) at the appropriate R.A. range to match our observations. Forming power spectra from these visibilities allowed for a comparison of our data to a ‘leakage only’ regime. We discuss the process for forming power spectra in Section 3.3, and the simulated power spectra are shown in comparison to those from data in Section 4.

## 2.2. Direction-Independent Leakage

In addition to the mixing of Stokes parameters due to the primary beam, it is possible to mix them in a direction independent way. Calibration errors are capable of leaking signal between pseudo-Stokes visibilities independent of the sky (Thompson et al. 2008). Again focusing on the  $I \rightarrow I, Q, U, V$  component of this leakage:  $V^I \rightarrow V^Q$  occurs through errors in calibrating the complex voltage gain factors for each dipole arm,  $V^I \rightarrow V^U$  occurs through the sum of off-diagonal gain terms ( $D$ -terms; the receptivity of dipole arm ‘n’ to an electric field vector aligned with arm ‘e’ and vice versa), and  $V^I \rightarrow V^V$  occurs through the difference in  $D$ -terms between two feeds.

**Table 1.** Observational parameters used for this study.

| Parameter             | Value                                      |
|-----------------------|--|
| JD range              | 2457548 – 2457555                          |
| LST Range             | 11 – 23 hrs                                |
| Frequency range       | 100 – 200 MHz                              |
| Frequency resolution  | 100 kHz                                    |
| Integration time      | 10 s                                       |
| Element diameter      | 14.7 m                                     |
| Number of elements    | 15   |
| Primary beam diameter | 9°   |
| System Temperature    | $100 + 120(\nu/150 \text{ MHz})^{-2.55}$ K |
| SEFD per element      | ~ 5800 Jy at 150 MHz                       |

We neglect calibration errors, and hence direction-independent leakage, in our simulations in order to build intuition around power spectrum estimates for a “perfectly behaving” instrument.

## 3. OBSERVATIONS AND REDUCTION

In this work we used eight nights of observations from the HERA-19 commissioning array. HERA is a low-frequency interferometer composed of 14 m-diameter dishes arranged in a close-packed hexagonal array of 14.7 m spacing. The commissioning array consists of nineteen dishes (see Figure 2); HERA is being constructed in staged build-outs, and upon completion will consist of 350 dishes in a fractured hexagon configuration (see Dillon & Parsons 2016; DeBoer et al. 2017). A feed cage containing two dipole feeds (recycled from the PAPER array, see Parsons et al. 2010), oriented in North-South and East-West directions, is suspended above each dish (Neben et al. 2016; Ewall-Wice et al. 2016b; Thyagarajan et al. 2016).

HERA only observes in drift-scan mode. The observations we used were eight nights, from Julian Date (JD) 2457548 to 2457555; LSTs 10.5 – 23 hr. Drift-scan visibilities were recorded every 10.7 seconds for 1024 evenly-spaced channels across the 100-200 MHz bandwidth. These data were divided into MIRIAD data sets roughly 10 minutes long. A night’s observation lasted 12 hours in total (6pm to 6am South African Standard Time; SAST); of these we used the central 10 hours, to avoid the Sun. **The details of our observations are summarized in Table 1.**

### 3.1. RFI Excision

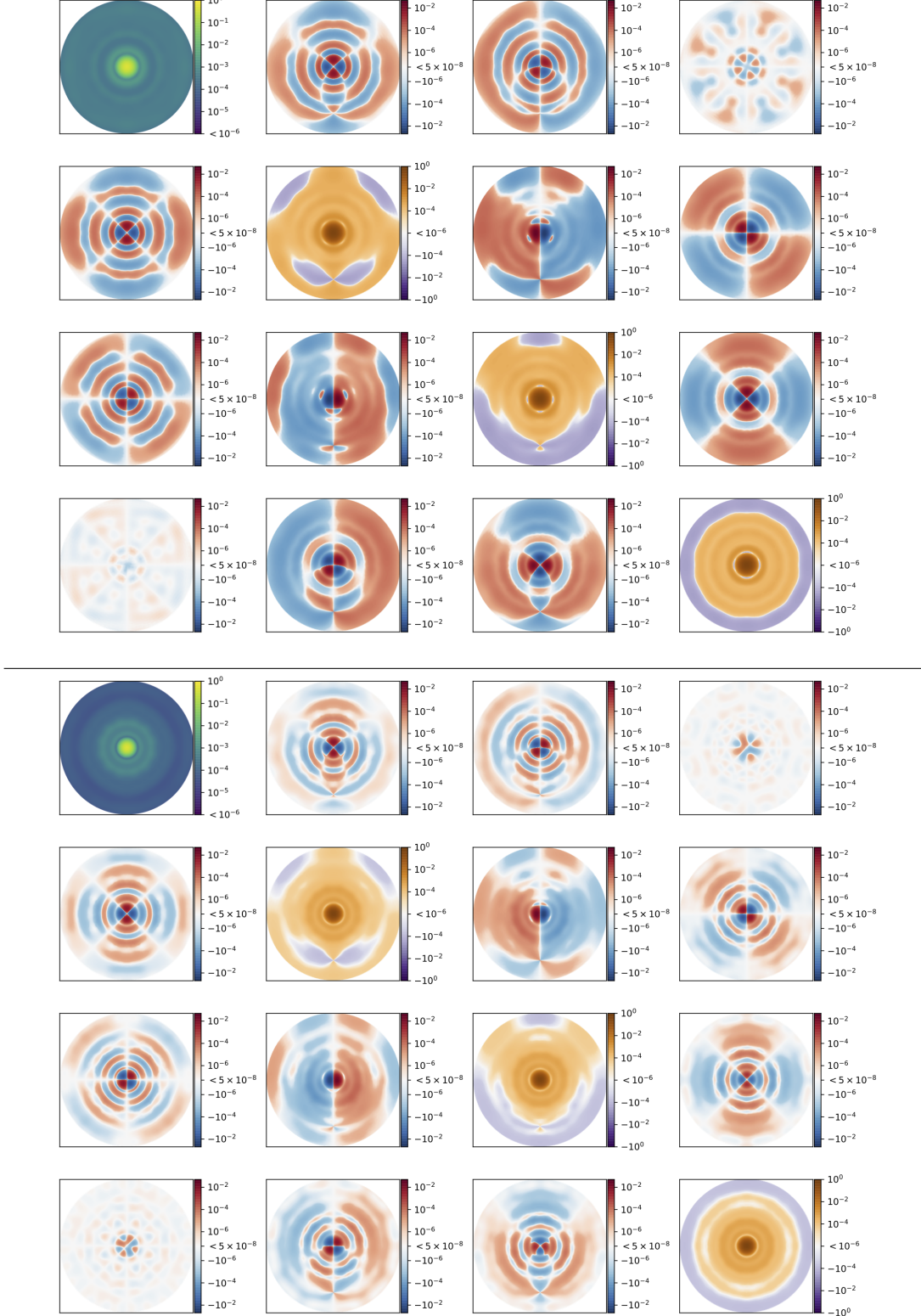


**Figure 1.** Simulations of the instrumental direction dependent Mueller matrix at 120 MHz and 160 MHz (*above* and *below*, respectively) projected into the RA, Dec basis. Color scales for frequencies are relative to the peak of  $\mathcal{M}_{00}$  (which itself is normalized to 1 at zenith). To account for the wide variety of dynamic ranges required to show detail, we use separate color maps for  $\mathcal{M}_{00}$ , diagonal, and off-diagonal terms. The off-diagonal terms are 2- to 8-orders of magnitude less than the diagonal terms. For a key to these matrices, see Equation 9.

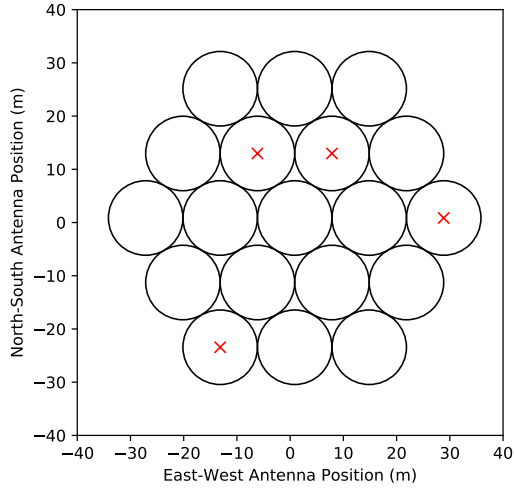


**Figure 2.** The perimeter of each dish in the HERA-19 array. A red "X" marks antennae that were identified during preprocessing and calibration as malfunctioning and were excluded from further analysis.

To identify samples contaminated by radio frequency interference (RFI), a two-dimensional median filter in time and frequency was applied to the visibility data to smooth out high pixel-to-pixel variations, and remove significant outliers that were likely unphysical. The variance of the resulting data was computed, and points with a  $z$ -score greater than 6 (i.e., points where the value is more than  $6\sigma$  away from the mean) were flagged as initial seeds for RFI extraction. A two-dimensional watershed algorithm was applied using these seeds as starting points, enlarging the regions of RFI-contamination to neighboring pixels with  $z$ -scores greater than 2, until all such pixels were flagged. Figure 3 shows the fractional RFI flag occupancy per time (displayed in LST) and frequency across the 8 days of observations. The majority of the band is relatively clear of RFI. Some clear features are: the FM radio band (below 110 MHz), ORBCOMM satellite communications (137 MHz), an ISS downlink (150 MHz) and VHF TV channels (above 170 MHz)<sup>7</sup>. The Galaxy, when transiting zenith at  $LST \approx 17.75$  hours, is so bright that it appears to degrade our ability to flag RFI.

### 3.2. Calibration

HERA is designed to be calibrated using redundant calibration techniques (Dillon & Parsons 2016), but for this preliminary view of HERA commissioning data,

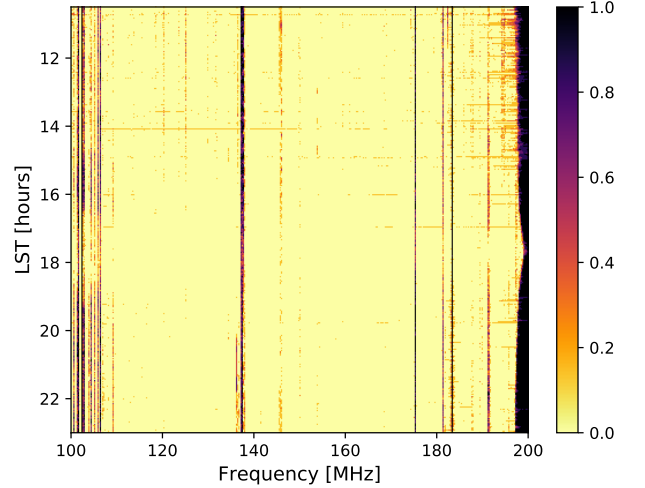


**Figure 3.** Fractional RFI flag occupancy per time and frequency over the eight days of observations. RFI was flagged on a per-(time,frequency) sample basis.

we used image-based calibration. Future studies with deeper integrations targeting EoR detections will take advantage of redundancy to obtain more precise calibration solutions (DeBoer et al. 2017). We used the CASA (McMullin et al. 2007) package for calibration, taking advantage of its CLEAN, gaincal and bandpass functions.

To enable the use of CASA, we first converted from native MIRIAD to a UVFITS file format which could be ingested by CASA using PYUVDATA (Hazelton et al. 2017). Using LSTs in which the Galactic center (GC;  $\alpha, \delta = 17h 45m 40.04s, -29d 0m 28.12s$ ) was transiting, we built a CLEAN model which modeled the GC as an unpolarized point source of strength 1 Jy and flat spectrum, which could be scaled appropriately later (see Equation 11). Clearly, this is an incomplete calibration model. However, as the objective of this work is to explore the response of the instrument in power spectrum space without combining baselines of different lengths, most of the purpose of the calibration **was** correcting an initial large cable delay per antenna. Treating the GC as unpolarized is adequate for this study. The large optical depth towards the GC (Oppermann et al. 2012) results in large amounts depolarization in the plane of the Galaxy (Wolleben et al. 2006). Moreover, we expected non-negligible amounts of beam depolarization due to the large solid angle of the synthesized beam.

For each night of observations, we used the CASA gaincal and bandpass functions to obtain **per-frequency channel** phase and amplitude solutions for each antenna and dipole arm **at the ten minute**

<sup>7</sup> For an extended discussion of RFI as seen by HERA, see the public [HERA Memo #19](#)

**interval corresponding to the transit of the GC. These routines used the GC model described above to form simulated visibilities, which could subsequently be fit to the data to determine the complex gains per antenna. The complex gain spectra per antenna were applied to the entire night of observations.** Four antennae had very deviant solutions, and their inclusion resulted in low-quality images. These were omitted from further analysis (and are marked with red “X”’s in Figure 2). Before calibration, we manually flagged the edges of the band (below 110 MHz and above 190 MHz), where spectral behavior is dominated by the high and low pass filtering in the HERA signal chain (DeBoer et al. 2017).

In Figure 4, we show images formed from the simulated pseudo-Stokes visibilities (top panels) and our observations (bottom panels). These are multi-frequency synthesis images, where we used all unflagged frequencies on either side of the band edges; 115 MHz to 188 MHz. We do not specify a beam model during imaging. **All images shown were produced using the ten minute interval used for calibration.** At HERA’s position ((latitude, longitude) = (-30:43:17.5, 21:25:41.9)) the Galactic Center transits  $2^\circ$  from zenith, while the HERA primary beam has a FWHM of  $\sim 5^\circ$  at 150 MHz (Neben et al. 2016). For the simulated visibilities, we flagged the same antennae as in the data. As expected for a compact array, the Stokes I images capture only a low-resolution view of the Galactic Center. The simulated and observed visibilities form remarkably similar images in Stokes I, Q and U, but the simulation under-predicts pseudo-Stokes V power. We defer further discussion to Section 4.

Example bandpass solutions from JD 2457548 are shown in Figure 5. Although some residual RFI remains obvious, the derived bandpasses were smooth. Thus, even though the gains were imprecise, we expected that using them should not add additional spectral structure. **The  $\sim 6$  dB spread in bandpass amplitudes is within the expected range for the electronics used in the analog signal chain (e.g. DeBoer et al. 2017).**

The complex gain solutions were subsequently applied to the MIRIAD files. Figure 6 shows the effect of calibration on the visibilities of three nominally redundantly-spaced baselines. Shown in that figure are the phases of three  $V^{nn}$  visibilities from 14.7 m baselines before and after calibration. There were no shared antennae between the visibilities shown. The qualitative agreement is obvious, providing a consistency check on the solutions.

We did not attempt to calibrate  $D$ -terms in this work.

We down-selected to two relatively RFI-free 20 MHz sub-bands (Figure 3); 115 to 135 MHz and 152 to 172 MHz, henceforth referred to the “low band” and the “high band”. As we discuss in Section 3.3, these bands were multiplied by a Blackman-Harris window, centered on their central frequencies, before Fourier transforming in order to minimize side-lobes. This windowing lead to an noise-effective bandwidth of 10 MHz, appropriate for EoR analyses since the HI signal is to a reasonable approximation coeval over the corresponding redshift range (Furlanetto et al. 2006).

Pseudo-Stokes visibilities were formed from the instrumental polarizations, following Equation 10. These visibilities were then scaled to the appropriate amplitude using a model for the GC spectrum

$$S_{\text{SgrA}^*}(\nu) \approx 3709 \text{ Jy} \times (\nu/408 \text{ MHz})^{-0.5} \quad (11)$$

drawn from the Global Sky Model (GSM; de Oliveira-Costa et al. 2008; Price 2016; Zheng et al. 2017). Note that the GSM is inherently  $\sim 5\%$  uncertain at these frequencies. We note that this scaling is heavily resolution dependent; we are treating the Galactic Center as a point source when it is extended in reality. However, Section 4 we show that we obtain sensible power levels for the foregrounds and noise, lending confidence to our overall scaling.

### 3.3. Forming power spectra

Power spectra were formed according to the method used in Pober et al. (2013) and Kohn et al. (2016), which we briefly review here. All Fourier transforms were windowed using a Blackman-Harris window at the center of the sub-band, which minimized sidelobes. Parsons et al. (2012b) define the *delay transform* as the Fourier transform of a visibility for baseline  $ij$  and pseudo-Stokes parameter  $P$  along the frequency axis

$$\tilde{V}_{ij}^P(\tau, t) = \int d\nu \tilde{V}_{ij}^P(\nu, t) e^{2\pi i \nu \tau}. \quad (12)$$

We note that using a Blackman-Harris window will induce a correlation between consecutive  $\tau$  modes. The Fourier transform of the window function in frequency will be sharply peaked in the delay space, and can be ignored to some extent. Hence the self-correlation of  $V_{ij}^P(\tau, t)$  can be used to define the power spectrum, although the small correlation of different  $\tau$  modes could effect the variance of the power spectrum (Parsons et al. 2014).

The power at each delay-mode and baseline can be represented in terms of their respective Fourier components  $k_{\parallel}$  and  $k_{\perp}$  (Parsons et al. 2012b; Thyagarajan

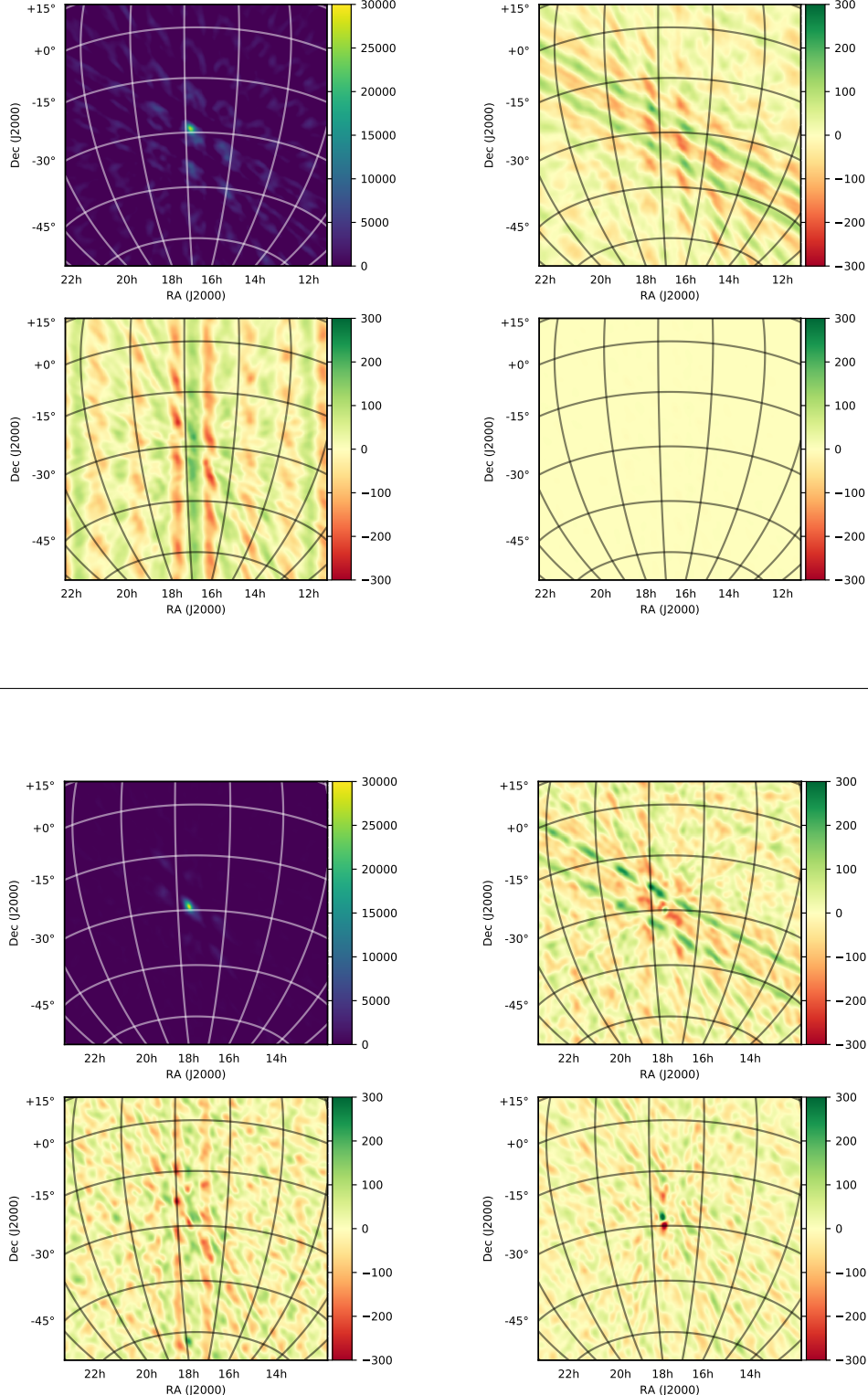


**Figure 4.** *Above:* Multi-frequency synthesis pseudo-Stokes images formed from simulation, where only a Stokes I sky was used; any polarized power is due to direction-dependent polarization leakage (see Section 2.1). *Below:* Multi-frequency synthesis pseudo-Stokes images formed from observed visibilities on JD 2457548. Both sets of panels show the Galactic Center (our calibrator source) close to transit in pseudo-Stokes I, Q, U and V visibilities (*top left*, *top right*, *lower left*, *lower right*). A Briggs-weighting with robustness 0 was used when gridding into the image plane. No deconvolution was performed. The colorbar is in units of Jy/Beam. A separate color scale is used for Stokes I for suitable dynamic range. An R.A., Dec. grid is shown, illustrating the wide-field nature of HERA observations.

et al. 2015a):

$$P(k_{\parallel}, k_{\perp}) \approx |\tilde{V}_{ij}^P(\tau)|^2 \frac{X^2 Y}{\Omega B} \left( \frac{c^2}{2k_B\nu^2} \right)^2,$$

$$k_{\parallel} = \frac{2\pi\nu_{21\text{cm}}H(z)}{c(1+z)^2}\tau,$$

$$k_{\perp} = \frac{2\pi}{D(z)\lambda}b$$

(13)

**Figure 5.** Bandpass solutions for the North-South dipole orientation obtained for the functioning antennae in the array on JD 2457548. Differences in line color and style is merely to distinguish different antennae. Shaded regions indicate the effective sub-bands used for power spectrum analysis.

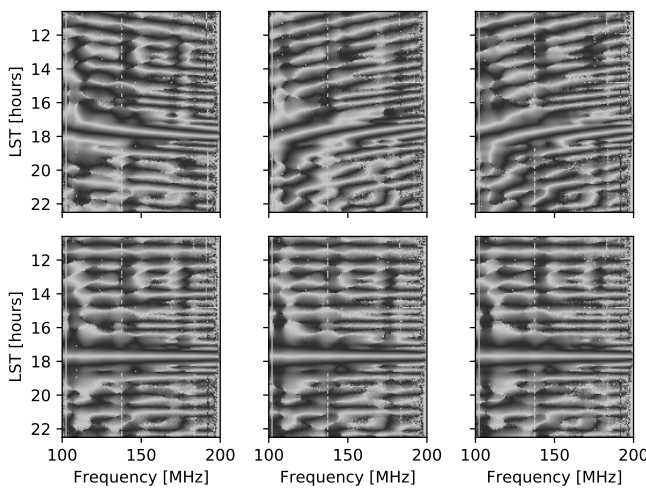


**Figure 6.** The effect of calibration on the phases of visibilities from three redundantly-spaced 14.7 m baselines; *nn* polarization. The color scale is cyclic; black is  $\pm\pi/2$  and white is 0 and  $\pm\pi$ . *Above:* before calibration; *below:* after calibration. A simple sky model was sufficient to enforce redundancy for redundant baselines.

for: bandwidth  $B$ , angular area of the beam  $\Omega$ ,  $\nu_{21\text{cm}} \approx 1420$  MHz, baseline length  $b$ , wavelength of observation  $\lambda$ , Hubble parameter  $H(z)$ , transverse comoving distance  $D(z)$  and redshift-dependent scalars  $X$  and  $Y$  (Parsons et al. 2012a). Note that the angular area of the beam refers to the diagonal components of the Mueller matrices shown in Figure 1. For further discussion of forming polarized power spectra in  $k$ -space, refer to Nunhokee et al. (2017).

To avoid a noise-bias when forming the  $|\tilde{V}_{ij}^P(\tau, t)|^2$  term, we cross-multiplied consecutive integrations, rephasing the zenith angle of the latter to the former:

$$|\tilde{V}_{ij}^P(\tau, t)|^2 \approx |\tilde{V}_{ij}^P(\tau, t) \times \tilde{V}_{ij}^P(\tau, t + \Delta t) e^{i\theta_{ij,\text{zen}}(\Delta t)}| \quad (14)$$

where  $\theta_{ij,\text{zen}}(\Delta t)$  was the appropriate phasing for baseline  $ij$  and  $\Delta t = 10.7$  seconds.

Pseudo-stokes power spectra were formed for each pair of integrations, for every baseline. After forming power spectra, baselines of identical lengths were averaged together **for all observation times**. Appealing to cosmological isotropy, baselines of the same length but different orientation should be sampling the same cosmological structure. These 2D power spectra were averaged over our 8 days of observations. Note that all averaging was performed after forming power spectra; this incoherent averaging was non-optimal from a signal-to-noise perspective outside the wedge, slightly reducing our sensitivity in the EoR window. However, the intention of this investigation was not a deep integration on noise; we were more interested in the polarized response of the instrument. As such, the power spectra presented in the Section below should be interpreted as approximate.

#### 4. RESULTS & DISCUSSION

Power spectra are shown for the high and low bands in Figure 7 and Figure 8, respectively, where white dotted lines mark the boundary of the EoR window on the 2D plots. The same data are presented in middle and lower

panels, with the latter overlaid as lines to emphasize common features of the power spectra with respect to baseline length.

Theoretical noise levels for the high and low bands were between  $P_{\text{noise}}(k) \approx 1.7 \times 10^8 \text{ mK}^2 \text{Mpc}^3 \text{h}^{-3}$  and  $3.4 \times 10^9 \text{ mK}^2 \text{Mpc}^3 \text{h}^{-3}$  in the high band, and between  $2.3 \times 10^8 \text{ mK}^2 \text{Mpc}^3 \text{h}^{-3}$  and  $6.1 \times 10^9 \text{ mK}^2 \text{Mpc}^3 \text{h}^{-3}$  in the low band. These estimates used a temperature model of the sky

$$T_{\text{sky}} = 180 \text{ K} \left( \frac{\nu}{180 \text{ MHz}} \right)^{-2.55}, \quad (15)$$

**assuming** receiver temperatures of 300 K and 600 K for the high band and low band, respectively (DeBoer et al. 2017, also see the public [HERA Memo #16](#)), and were calculated according to the formalism for noise power spectra in Parsons et al. (2012b), with the inclusion of a baseline-number dependence:

$$P_{\text{Noise}}(k) \approx \frac{1}{2\Delta t \sqrt{N_{\text{LST}}} N_{\text{days}} N_{\text{bl}}} X^2 Y B_{\text{NE}} \Omega_{\text{eff}} T_{\text{sys}}^2. \quad (16)$$

In the above equation,  $\Delta t$  is integration time,  $N_{\text{LST}}$  is the number of LST hours used per day (12 hours),  $N_{\text{bl}}$  is the number of baselines (which differed per  $k_{\perp}$  bin),  $X$  and  $Y$  are cosmological scalars defined in Parsons et al. (2012b),  $B_{\text{NE}}$  is the noise equivalent bandwidth and  $\Omega_{\text{eff}}$  is the effective beam area, as defined in Parsons et al. (2014).

These noise power estimates were roughly corroborated by our observations (see Figure 9). We observe excess noise on the shortest baselines (also obvious in the lower panels of Figures 7 and 8).

#### 4.1. General features of the power spectra

The most striking feature of these power spectra is the degree of foreground isolation achieved in all pseudo-Stokes parameters. In a similar study of 2D polarized power spectra, PAPER (Kohn et al. 2016) measurements showed a “filled” region of Fourier space out to the edge of the EoR window (in the delay-spectrum paradigm, this corresponds to the horizon; zenith angle  $\pm 90^\circ$ ), with some supra-horizon leakage (Pober et al. 2013) into the EoR window itself. The power spectra in Figures 7 and 8 show no such behavior; all foreground emission appears to be contained within a narrow region around  $k_{\parallel} = 0 \text{ h/Mpc}$ . This behavior was predicted for an array of HERA-like dishes by Thyagarajan et al. 2015a (although that study only concentrated on the Stokes I component).

Power at horizon delays, as predicted by Thyagarajan et al. (2015a) and Neben et al. (2016), was not observed.

This was likely a resolution effect. To resolve horizon-delay power, one would need to sample many periods of  $\tau_h = b/c$ , where  $b$  is the magnitude of the baseline vector. The maximum length baseline in the HERA-19 array was 58.4 m, corresponding to a  $\sim 5$  MHz period: barely sampled by the 10 MHz windows we use in this study. The lack of horizon power is corroborated by the simulations of the HERA delay response in Ewall-Wice et al. (2016b) and Thyagarajan et al. (2016), although those studies used a different windowing function for the delay transform. Their simulations also predict a high degree of foreground isolation: the presence of noise in our data of course meant that we do not realize the 11 dex of isolation that can be achieved in simulation, but the  $\sim 8$  dex we do see, without any foreground subtraction and a simple calibration, speaks to the power of HERA’s future capabilities.

Visible in the observational data, but not in the simulation, is an excess of power at  $k_{\parallel} = 0.04 \text{ h/Mpc}$ , corresponding to a delay of 100 ns, which is independent of baseline length. This suggests that its origins are in the HERA signal chain. There are 15 m coaxial cables at one stage of the signal chain from the HERA dishes to the correlator<sup>8</sup>. In the limit of little delay induced by the cable and our limited delay resolution, a reflection along this stage of the signal chain would produce an alias of the foreground signal at a  $\tau \approx 100$  ns (Beardsley et al. 2016; Ewall-Wice et al. 2016a).

#### 4.2. Day-to-day variability

The foreground and EoR window power levels appeared to be relatively stable between days, with variation most likely due to the incomplete sky model used for gain calibration. Figure 9 shows power as a function of baseline length for  $k_{\parallel} = 0 \text{ h/Mpc}$  (solid lines) and  $k_{\parallel} = 0.2 \text{ h/Mpc}$  (dot-dashed lines). Deviations from the mean at  $k_{\parallel} = 0 \text{ h/Mpc}$  may be a limitation imposed by our simplistic sky model. Since the noise levels in the EoR window region remained noise-like throughout our observations, the uncertainty in the absolute gain scale did not have a large impact on our largely-diagnostic investigation.

#### 4.3. Polarimetric results

Figures 7 and 8 qualitatively illustrate that the simulations described in Section 2.1 reproduced the main features of the observed power spectra. The simulations were run only with a Stokes I sky component and no

<sup>8</sup> This stage of the signal chain is only present in the commissioning array. Future HERA build-outs will transition to a different architecture (DeBoer et al. 2017).

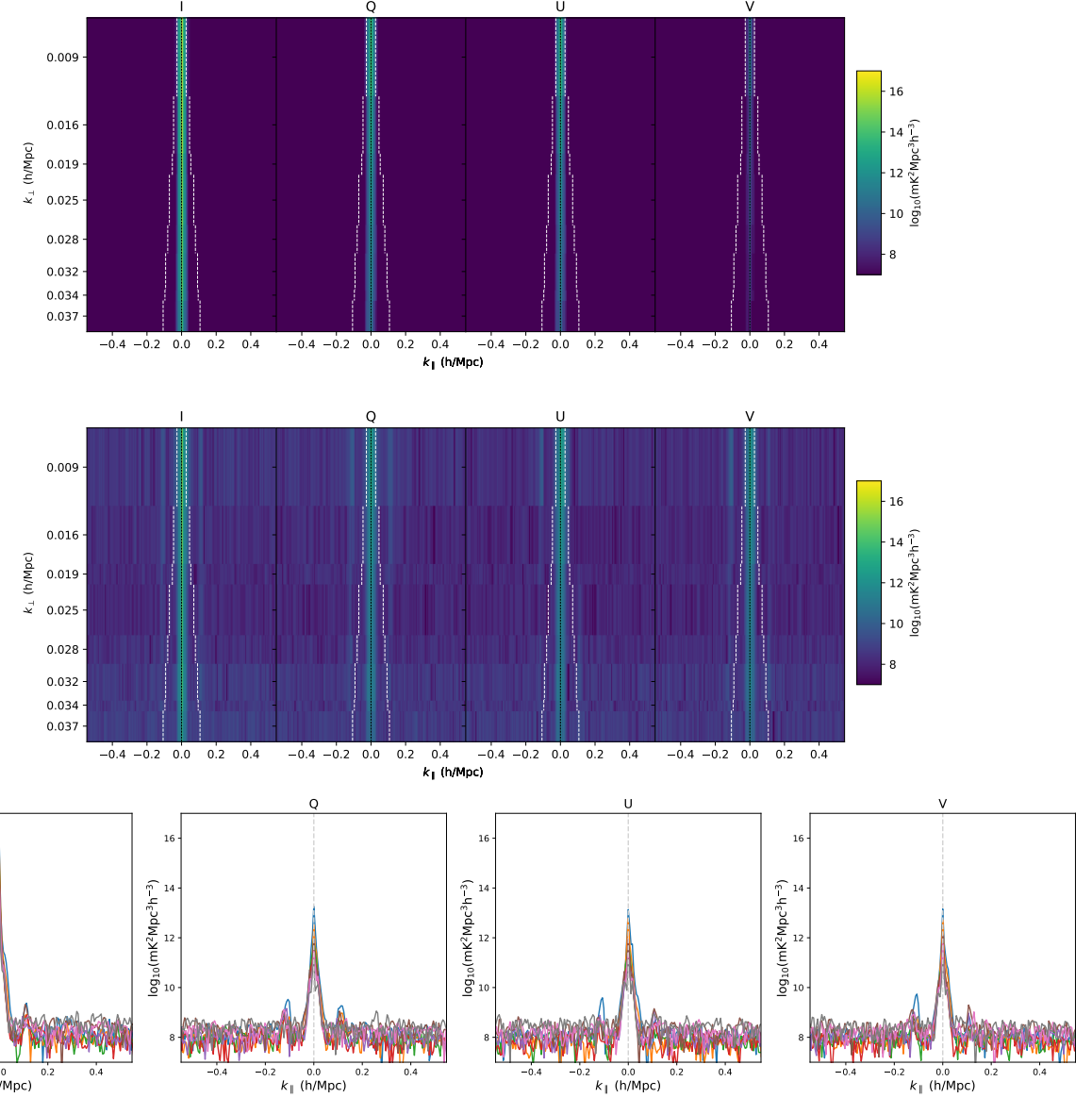


**Figure 7.** Results from the high-band (157–167 MHz). White dotted lines indicate the boundary of the pitchfork and the EoR window. A black dotted line indicates the  $k_{\parallel} = 0$  h/Mpc line. *Top:* Simulated power spectra in Stokes I, Q, U and V, following the formalism in Section 2 – no polarized sky model was used, so power in Stokes Q, U and V was only due to direction-dependent leakage from Stokes I. No instrumental noise was included in the simulation. *Middle:* Eight-day average power spectra from data. *Bottom:* The same data as shown in the middle panel, but with each baseline length overlaid on one another to allow shared features to be more easily identified.

simulated calibration errors, so the only signal in the polarized power spectra was from wide-field beam leakage (Figure 1). An example comparison between simulation and observation in the image plane is shown in Figure 4.

In Figure 10 we show the power levels observed on the shortest baseline (14.7 m) compared to our simulations for each band. The simulations used an unpolarized diffuse sky model (the most recent version of the GSM; Zheng et al. 2017), which should be accurate at the scales probed by a 14.7 m baseline. We saw that the simulations reproduced  $\sim 75\%$  of the foreground power observed in pseudo-Stokes I in the high band, and overpredicted foreground power by  $\sim 35\%$  in the low band. This could have been due to unrealistic frequency scaling of the diffuse foregrounds in the GSM.

For pseudo-Stokes Q and U, the simulations accounted for  $\sim 60 - 75\%$  of power seen within the pitchfork region, suggesting that most of the power seen in these power spectra, at least for the shortest baselines, can be mostly attributed to direction-dependent leakage effects. **Residual gain and phase errors are able to leak a fraction of pseudo-Stokes I into Q and U in a direction-independent fashion. There is excess power close to the location of the Galactic Center, and increased power over the sky, in the observed pseudo-Stokes Q and U skies compared to the simulated ones in Figure 4. Recall that the simulated pseudo-Stokes Q and U images contain only direction-dependent leakage from Stokes I. As the Galactic Center is the highest-amplitude source of power, we expect residual gain errors to be most obvious in the same position as it is in the pseudo-Stokes I image. Such an excess is indeed present in the observed pseudo-Stokes Q and U images, but absent in the simulated ones – pointing to direction-independent gain errors being present.**

**Some fraction of the observed power ( $\leq 25\%$ ; the excess in polarized power above predicted leakage levels) may have been due to linearly polarized foregrounds. Referring to Figure 10, the measured ratio of the pseudo-Stokes Q and U power spectra to pseudo-Stokes I was roughly 2.5 dex. Removing the expected  $\sim 75\%$  of power attributed to direction-dependent leakage, and assuming the remainder to be intrinsically polarized power rather than direction-independent gain errors, corresponded to an intrinsic polarized fraction of  $\sim 0.03$ . This would represent polarized fluctuations measured by the shortest baseline to be on the order of  $\sim 5\text{K}$ , consistent with measurements of large-scale polar-**

**ized structures by Jelić et al. (2015) and Lenc et al. (2016). To disentangle the contribution of gain errors and intrinsic polarization to the observed power requires more substantial simulation and statistical subtraction efforts (e.g. Lenc et al. 2018), which is outside the scope of this paper, and we defer to future work.**

The observed pseudo-Stokes V power spectrum was more poorly modelled by our simulation. In both bands we observed  $\sim 20$  dB more power in pseudo-Stokes V at  $k_{\parallel} = 0 \text{ h/Mpc}$  than predicted by our simulations. The peak power observed in pseudo-Stokes V was roughly 0.1% of the peak power observed in pseudo-Stokes I. Likewise in the sky images shown in Figure 4, there is little pseudo-Stokes V power in the simulated images, compared to observation. This suggests that most or all of the power in pseudo-Stokes V is due to direction independent leakage. While the leakage appears localized in Figure 4, we see in Figure 10 that it is statistically similar to pseudo-Stokes Q and U in power. Since  $D$ -terms cause direction-independent leakage from pseudo-Stokes I to pseudo-Stokes V, the excess power we observed could be interpreted as an approximate  $D$ -term level of  $\sim 1\%$  (Thompson et al. 2008). This is similar to  $D$ -term levels from other low frequency instruments such as MWA-32, which was found to have  $\sim 2\%$   $D$ -terms (G. Bernardi, private communication). To understand which effect, if either, is dominant, a precise  $D$ -term calibration of HERA is required. This effort is underway with data taken with bright polarized point sources in transit, and will be presented in future work. Another potential cause of the discrepancy could have been that our simulations under-predicted Stokes V power, due to lack of accounting for some variety of instrumental circular polarization.

In Section 4.1 we noted the presence of excess power at  $k_{\parallel} = \pm 0.04 \text{ h/Mpc}$  ( $\pm 100 \text{ ns}$ ) that was independent of baseline length, suggesting that it was due to a reflection along 15 m cables. Figure 10 shows that power at this delay is not consistent between polarizations. Stokes U and V power only exhibited excess signal at  $-100 \text{ ns}$  in the high band, and in the low band, it was only Stokes U that did not exhibit that excess at  $+100 \text{ ns}$ . This may be a clue about the polarization state of cable reflections, perhaps as a function of frequency, but we defer this to future work – noting it as a point of interest here.

## 5. CONCLUSIONS

In this work we have presented polarized power spectra from the HERA-19 commissioning array. With modest calibration, HERA is able isolate total intensity and

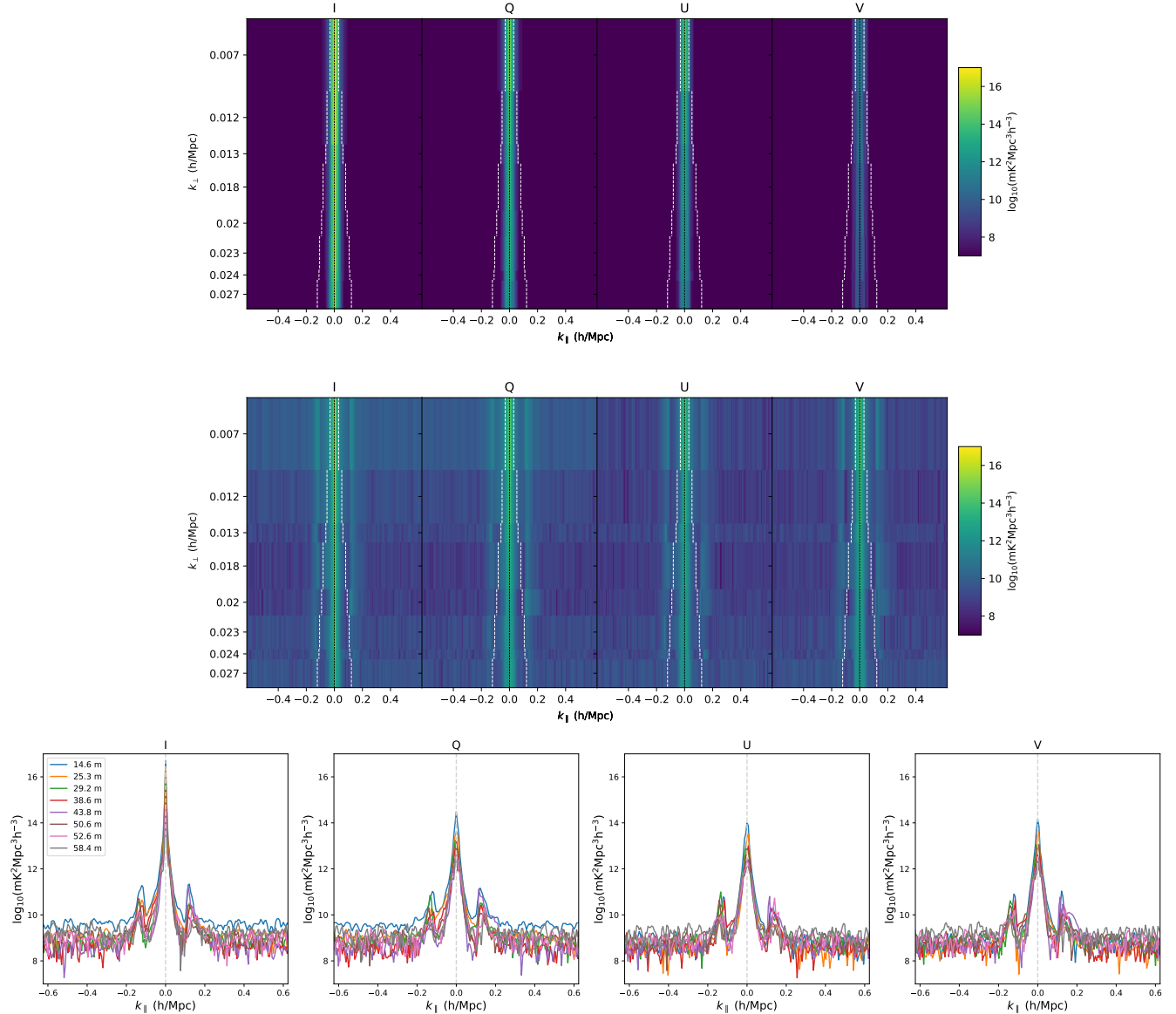


**Figure 8.** Results from the low-band (120–130 MHz), arranged in the same format as Figure 7.

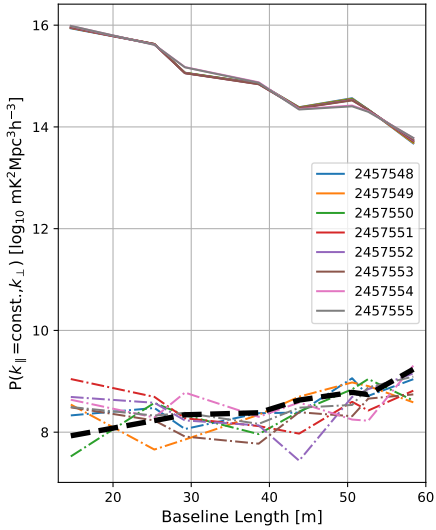


**Figure 9.** High band power as a function of baseline length for the center of the pitchfork ( $k_{\parallel} = 0$  h/Mpc; solid lines) and in the EoR window ( $k_{\parallel} = 0.2$  h/Mpc; dot-dashed lines) for **pseudo-Stokes I** on each JD of observation. The black dashed line represents the approximate noise power assuming a receiver temperature of 300 K. A very similar relationship is shown in the low band, but with a higher noise floor, which is consistent with system temperature as a function of frequency. The noise level climbs with baseline length as the compact nature of the array gives more short baselines to average-over in a given ( $k_{\parallel}, k_{\perp}$ ) bin than longer ones.

polarized foregrounds to within the “pitchfork” region of  $k$ -space, as predicted by Thyagarajan et al. (2015a), lending confidence to its future performance as an instrument capable of both detecting and characterizing the EoR power spectrum. Of course, the array used in this study had just 19 antennae, 15 of which were used for analysis – future build-outs of HERA with up to 350 antennae will require strong quality-assurance efforts.

Simulations of the polarized response of the instrument, mapped into the same Fourier space as the data, suggest that most or all of the polarized power observed in pseudo-Stokes Q and U power spectra is due to direction-dependent beam leakage from pseudo-Stokes I. Residual gain and phase errors could account for the rest of the power, but some fraction of the total ( $\leq 25\%$ ) may be due to linearly polarized foregrounds. Excess power in pseudo-Stokes V may be due to  $D$ -terms at the 1% level, but a full image-based calibration with a polarized point source is required to confirm this. The general accuracy of our simulations suggests current modelling of the complex HERA beam is accurate.

Much of this study was undertaken during the inaugural CAMPARE-HERA Astronomy Minority Partnership (CHAMP). This material is based upon work supported by the National Science Foundation under Grant Nos. 1440343 and 1636646, the Gordon and Betty Moore Foundation, and institutional support from the HERA collaboration partners. SAK is supported by a University of Pennsylvania SAS Dissertation Completion Fellowship. JEA acknowledges support from NSF CAREER award # 1455151. C.D.N. is supported by the SKA SA scholarship program. AL acknowledges support for this work by NASA through Hubble Fellowship grant # HST-HF2-51363.001-A awarded by the Space Telescope Science Institute, which is operated by the Association of Universities for Research in Astronomy, Inc., for NASA, under contract NAS5-26555. G.B. acknowledges support from the Royal Society and the Newton Fund under grant NA150184. This work is based on the research supported in part by the National Research Foundation of South Africa (grant No. 103424). JSD acknowledges the support of the NSF AAPF award # 1701536 and the Berkeley Center for Cosmological Physics.

*Software:* This research made use of Astropy, a community-developed core Python package for Astronomy (Astropy Collaboration et al. 2013); CASA (McMullin et al. 2007); pyuvdata (Hazelton et al. 2017); pygsm (Price 2016)

## REFERENCES

- Asad, K. M. B., Koopmans, L. V. E., Jelić, V., et al. 2015, MNRAS, 451, 3709  
—. 2016, MNRAS, 462, 4482
- Astropy Collaboration, Robitaille, T. P., Tollerud, E. J., et al. 2013, A&A, 558, A33
- Beardsley, A. P., Hazelton, B. J., Sullivan, I. S., et al. 2016, ApJ, 833, 102
- Bernardi, G., de Bruyn, A. G., Brentjens, M. A., et al. 2009a, A&A, 500, 965  
—. 2009b, A&A, 500, 965
- Bernardi, G., de Bruyn, A. G., Harker, G., et al. 2010, A&A, 522, A67
- Bernardi, G., Greenhill, L. J., Mitchell, D. A., et al. 2013, ApJ, 771, 105

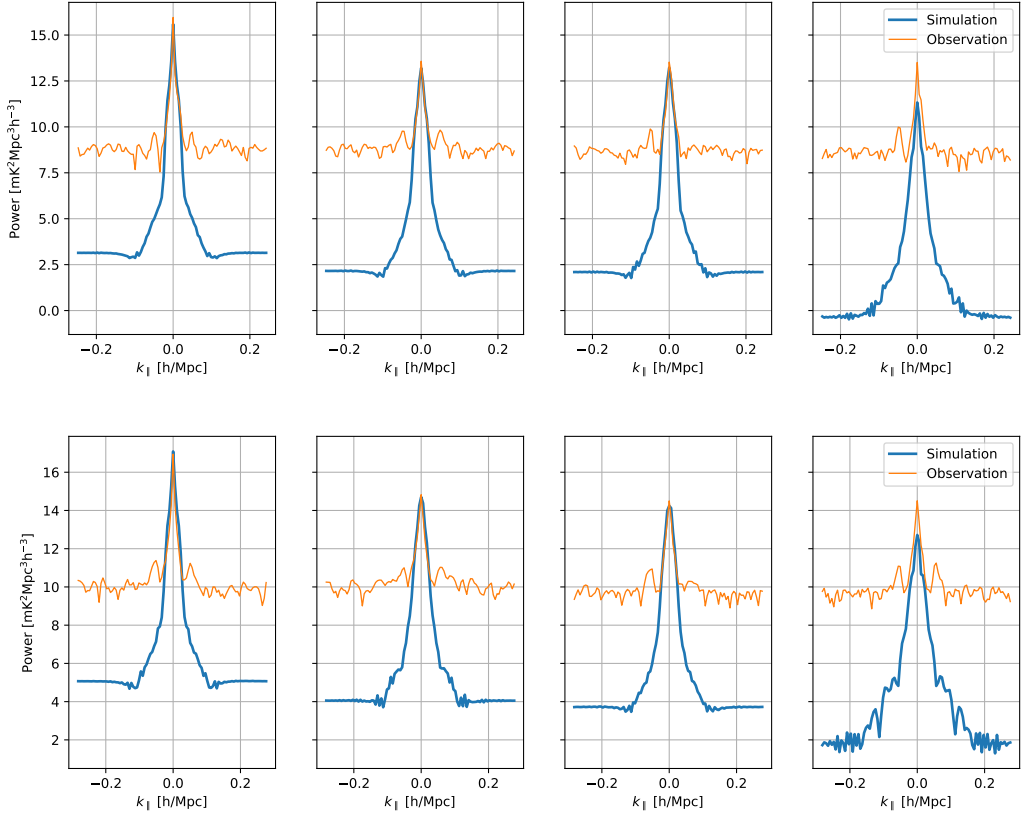


**Figure 10.** Simulated and observed power as a function of  $k_{\parallel}$  for the shortest baseline (14.7 m). *Right to left:* pseudo-Stokes I, Q, U and V; *above:* the high band; *below:* the low band. The simulations were noiseless and used an unpolarized sky model. They capture the foreground power levels in pseudo-Stokes I, Q and U, suggesting most power in Q and U is due to leakage from Stokes I. The power level in V is highly discrepant, however, suggesting some sort of beam-independent instrumental leakage.

- Carozzi, T. D., & Woan, G. 2009, MNRAS, 395  
 Datta, A., Bowman, J. D., & Carilli, C. L. 2010, ApJ, 724, 526  
 de Oliveira-Costa, A., Tegmark, M., Gaensler, B. M., et al. 2008, MNRAS, 388, 247  
 DeBoer, D. R., Parsons, A. R., Aguirre, J. E., et al. 2017, PASP, 129, 045001  
 Dillon, J. S., & Parsons, A. R. 2016, ApJ, 826, 181  
 Dillon, J. S., Liu, A., Williams, C. L., et al. 2014, PhRvD, 89, 023002  
 Dillon, J. S., Neben, A. R., Hewitt, J. N., et al. 2015a, PhRvD, 91, 123011  
 Dillon, J. S., Tegmark, M., Liu, A., et al. 2015b, PhRvD, 91, 023002  
 Ewall-Wice, A., Dillon, J. S., Hewitt, J. N., et al. 2016a, MNRAS, 460, 4320  
 Ewall-Wice, A., Bradley, R., Deboer, D., et al. 2016b, ApJ, 831, 196  
 Fagnoni, N., & de Lera Acedo, E. 2016, ArXiv e-prints, arXiv:1606.08701

- Farnes, J. S., Gaensler, B. M., & Carretti, E. 2014, ApJS, 212, 15  
 Furlanetto, S. R., Oh, S. P., & Briggs, F. H. 2006, PhR, 433, 181  
 Geil, P. M., Gaensler, B. M., & Wyithe, J. S. B. 2011, MNRAS, 418, 516  
 Hazelton, B., Beardsley, A., Pober, J., et al. 2017, HERA-Team/pyuvdata: Version 1.1, doi:10.5281/zenodo.546260  
 Jelić, V., de Bruyn, A. G., Mevius, M., et al. 2014, A& A, 568, A101  
 Jelić, V., de Bruyn, A. G., Pandey, V. N., et al. 2015, A& A, 583, A137  
 Kohn, S. A., Aguirre, J. E., Nunhokee, C. D., et al. 2016, ApJ, 823, 88  
 Lenc, E., Murphy, T., Lynch, C. R., Kaplan, D. L., & Zhang, S. 2018, ArXiv e-prints, arXiv:1805.05482  
 Lenc, E., Gaensler, B. M., Sun, X. H., et al. 2016, ApJ, 830, 38  
 Lenc, E., Anderson, C. S., Barry, N., et al. 2017, PASA, 34, e040

- Liu, A., Parsons, A. R., & Trott, C. M. 2014a, PhRvD, 90, 023018
- . 2014b, PhRvD, 90, 023019
- Ludwig, A. 1973, IEEE Transactions on Antennas and Propagation, 21, 116
- Martinot, Z. E., Aguirre, J. E., Kohn, S. A., & Washington, I. Q. 2018, ArXiv e-prints, arXiv:1808.05968
- McMullin, J. P., Waters, B., Schiebel, D., Young, W., & Golap, K. 2007, in Astronomical Data Analysis Software and Systems XVI, ed. R. A. Shaw, F. Hill, & D. J. Bell, 376, ASP, San Francisco, CA, 127
- Mishra, A., & Hirata, C. M. 2017, ArXiv e-prints, arXiv:1707.03514
- Moore, D. F., Aguirre, J. E., Parsons, A. R., Jacobs, D. C., & Pober, J. C. 2013, ApJ, 769, 154
- Moore, D. F., Aguirre, J. E., Kohn, S. A., et al. 2017, ApJ, 836, 154
- Morales, M. F., Hazelton, B., Sullivan, I., & Beardsley, A. 2012, ApJ, 752, 137
- Neben, A. R., Bradley, R. F., Hewitt, J. N., et al. 2016, ApJ, 826, 199
- Nunhokee, C. D., Bernardi, G., Kohn, S. A., et al. 2017, ApJ, 848, 47
- Oppermann, N., Junklewitz, H., Robbers, G., et al. 2012, A&A, 542, A93
- Parsons, A., Pober, J., McQuinn, M., Jacobs, D., & Aguirre, J. 2012a, ApJ, 753, 81
- Parsons, A. R., Pober, J. C., Aguirre, J. E., et al. 2012b, ApJ, 756, 165
- Parsons, A. R., Backer, D. C., Foster, G. S., et al. 2010, AJ, 139, 1468
- Parsons, A. R., Liu, A., Aguirre, J. E., et al. 2014, ApJ, 788, 106
- Planck Collaboration, Ade, P. A. R., Aghanim, N., et al. 2016, A& A, 594, A13
- Pober, J. C., Parsons, A. R., Aguirre, J. E., et al. 2013, ApJL, 768, L36
- Pober, J. C., Liu, A., Dillon, J. S., et al. 2014, ApJ, 782, 66
- Price, D. C. 2016, PyGSM: Python interface to the Global Sky Model, Astrophysics Source Code Library, ascl:1603.013
- Shaw, J. R., Sigurdson, K., Sitwell, M., Stebbins, A., & Pen, U.-L. 2015, PhRvD, 91, 083514
- Smirnov, O. M. 2011a, A& A, 527, A106
- . 2011b, A& A, 527, A107
- Thompson, A. R., Moran, J. M., & Swenson Jr, G. W. 2008, Interferometry and synthesis in radio astronomy (John Wiley & Sons)
- Thyagarajan, N., Parsons, A. R., DeBoer, D. R., et al. 2016, ApJ, 825, 9
- Thyagarajan, N., Udaya Shankar, N., Subrahmanyan, R., et al. 2013, ApJ, 776, 6
- Thyagarajan, N., Jacobs, D. C., Bowman, J. D., et al. 2015a, ApJL, 807, L28
- . 2015b, ApJ, 804, 14
- Trott, C. M., Wayth, R. B., & Tingay, S. J. 2012, ApJ, 757, 101
- van Straten, W., Manchester, R. N., Johnston, S., & Reynolds, J. E. 2010, PASA, 27, 104
- Vedantham, H., Udaya Shankar, N., & Subrahmanyan, R. 2012, ApJ, 745, 176
- Wolleben, M., Landecker, T. L., Reich, W., & Wielebinski, R. 2006, A& A, 448, 411
- Zheng, H., Tegmark, M., Dillon, J. S., et al. 2017, MNRAS, 464, 3486